Dual-energy X-ray analysis using synchrotron computed tomography at 35 and 60 keV for the estimation of photon interaction coefficients describing attenuation and energy absorption

Stewart Midgley[a]* and Nanette Schleich[b]

[a]School of Physics, Monash University, Clayton, VIC 3080, Australia, and [b]Department of Radiation Therapy, University of Otago, Wellington, New Zealand. *Correspondence e-mail: stewart.midgley@monash.edu

A novel method for dual-energy X-ray analysis (DEXA) is tested using measurements of the X-ray linear attenuation coefficient μ. The key is a mathematical model that describes elemental cross sections using a polynomial in atomic number. The model is combined with the mixture rule to describe μ for materials, using the same polynomial coefficients. Materials are characterized by their electron density N_e and statistical moments R_k describing their distribution of elements, analogous to the concept of effective atomic number. In an experiment with materials of known density and composition, measurements of μ are written as a system of linear simultaneous equations, which is solved for the polynomial coefficients. DEXA itself involves computed tomography (CT) scans at two energies to provide a system of non-linear simultaneous equations that are solved for N_e and the fourth statistical moment R_4. Results are presented for phantoms containing dilute salt solutions and for a biological specimen. The experiment identifies 1% systematic errors in the CT measurements, arising from third-harmonic radiation, and 20–30% noise, which is reduced to 3–5% by pre-processing with the median filter and careful choice of reconstruction parameters. DEXA accuracy is quantified for the phantom as the mean absolute differences for N_e and R_4: 0.8% and 1.0% for soft tissue and 1.2% and 0.8% for bone-like samples, respectively. The DEXA results for the biological specimen are combined with model coefficients obtained from the tabulations to predict μ and the mass energy absorption coefficient at energies of 10 keV to 20 MeV.

1. Introduction

Synchrotron light sources (Boldeman & Einfeld, 2004) combined with wavelength-dispersive X-ray optics, a sample-rotation stage and an area detector enable mono-energetic X-ray computed tomography (CT) studies with excellent spatial resolution (Stevenson *et al.*, 2012). The ability to rapidly change beam energy allows materials analysis based upon the energy and compositional dependence of the X-ray linear attenuation coefficient μ. Absorption-edge discontinuities can be exploited to quantify elemental concentration *via* methods such as K-edge subtraction (KES) (Zhu *et al.*, 2014). However, the K-edges for elements in biological samples are below 5 keV, so KES is restricted to very small samples (*e.g.* excised specimens) or introduced contrast agents. At higher energies, μ varies smoothly (*i.e.* with continuous first derivative), decreasing at higher energies E and increasing for higher atomic number Z materials, according to the power-law relationship Z^m/E^n where the photoelectric effect dominates (with m = 3–4 and n = 2–3) and the Klein–Nishina formula where incoherent scattering

35 keV 60 keV

Ne R4
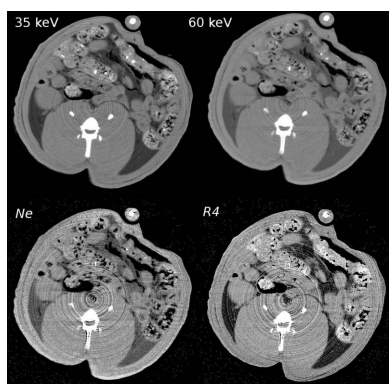
is important. Traditional methods of analysis utilize basis materials decomposition, which assumes that the sample is composed of only two or more materials. Measurements at different energies are written as linear simultaneous equations and solved for the contribution from each basis material.

We use a mathematical model describing the attenuation coefficient for materials proportional to electron density N_e and a non-linear function of elemental composition (Jackson & Hawkes, 1981; Torikoshi *et al.*, 2003; Midgley, 2004). For mixtures and compounds, the distribution of elements is described using statistical moments representing the mean atomic number, its variance, skewness and kurtosis. These moments account for the compositional dependence for each interaction process; atomic form factors (Hubbell & Överbö, 1979) and incoherent scattering factors (Hubbell *et al.*, 1975) have weak contributions from all moments, whilst the photo-electric effect is dominated by the fourth statistical moment R_4 which is related to the concept of effective atomic number (White, 1977; Jackson & Hawkes, 1981). §2.1 reviews the theoretical model describing μ for mixtures. Dual- and multiple-energy X-ray analysis (DEXA and MEXA) obtain measurements at two or more photon energies, which are written as simultaneous equations and then solved for N_e and R_4.

The energy absorption coefficient μ_{en} (Seltzer, 1993) is described by the same model. Both parameters μ and μ_{en} are required for radiation dosimetry calculations where μ accounts for attenuation and an estimate for the kinetic energy transferred to the medium (kerma) by the primary beam (Greening, 1981) is obtained *via*

$$K_{med} = \sum_E I_t(E) \left(\frac{\mu_{en}}{\rho} \right)_{med} E. \qquad (1)$$

In this expression, I_t is the transmitted beam fluence (number of photons per unit area) at depth in the medium with mass energy absorption coefficient $(\mu_{en}/\rho)_{med}$, and the summation is over the spectrum of beam energies. Calculation of absorbed dose must also account for scattered radiation arising from interactions at other locations and depths, whereby kerma is multiplied by the backscatter factor (BSF) estimated from measurements (Harrison, 1982) and *via* Monte Carlo methods. For diagnostic X-ray energies (approximately 20–150 keV) interacting with tissues, the BSF is unity for a pencil beam and approximately 1.10 to 1.35 for fan-beam to wide-beam conditions.

The aims of this study were to acquire CT data at diagnostic X-ray energies (*i.e.* suitable for animal or human imaging), against which to test our DEXA model and its applications for radiation dosimetry, namely predicting μ and (μ_{en}/ρ) over a broad range of photon energies. §2 describes the DEXA methodology, phantom design and methods for characterizing attenuation measured at the Australian Synchrotron Imaging and Medical Beamline (IMBL). §2.6 reviews the necessary CT data processing steps and quality control procedures for beamline characterization. The CT results for the phantoms and a biological specimen are presented in §3, where we

examine DEXA accuracy and predict interaction coefficients at photon energies of 10 keV to 20 MeV.

2. Materials and methods

The following sections review DEXA theory, describe the instrumentation for mono-energetic CT, the design of a phantom for characterizing measured attenuation, necessary quality control procedures for the experiment, CT data acquisition and processing methods.

2.1. Theory and mathematical methods for DEXA

The energy and compositional dependence of atomic cross sections σ can be described by non-linear and non-trivial mathematical expressions that account for each interaction process. Jackson & Hawkes (1981) used a Taylor expansion to third order to rewrite these expressions as separate functions of Z and E. Torikoshi *et al.* (2003) recast the parameterization of Jackson & Hawkes as a function of electron density, with composition expressed as a function of an effective atomic number (which is denoted R_4 below), plus further coefficients that represent photoelectric and scattering interactions. An alternative approach (Midgley, 2004) describes the compositional dependence of cross sections expressed per electron using a polynomial,

$$\sigma_e(Z) = S_1 + S_2 Z + S_3 Z^2 + S_4 Z^3 + \dots, \qquad (2)$$

where coefficients S_k are a function of photon energy. The attenuation coefficients for mixtures and compounds are obtained by combining this expression with the mixture rule. The constituent elements have atomic volume density $n_a(Z)$, and the material is characterized by the parameters

$$M_k = \sum_Z n_a(Z) Z^k = N_e R_k^{(k-1)}, \qquad (3)$$

where N_e is the electron density. The compositional parameters R_k have the same units as atomic number, analogous with the concept of effective atomic number (White, 1977), representing the statistical moments for variance, skewness and kurtosis. The model is written either as

$$\mu = S_1 M_1 + S_2 M_2 + S_3 M_3 + S_4 M_4 + \dots \qquad (4)$$

or as the non-linear expression

$$\mu = N_e \left(S_1 + S_2 R_2 + S_3 R_3^2 + S_4 R_4^3 + \dots \right) \qquad (5)$$

requiring four parameters for biological tissues at energies 30–150 keV, five coefficients at lower energies or for a broader compositional range, and fewer coefficients at higher energies. The parameters R_k are correlated (Midgley, 2011), so it is not possible to use equation (4) for multi-energy analysis (MEXA) and recover all compositional parameters (Midgley, 2005). Instead we rewrite the model as a function of R_4 attributed to the strong compositional contribution from photoelectric interactions, by introducing the ratios

$$f_k = \frac{R_k}{R_4}, \qquad (6)$$

which can be approximated by a constant or, for tissue, by a slowly varying function of R_4 (Midgley, 2011). With materials now characterized by just two parameters, DEXA uses the following non-linear model:

$$\mu(E) = N_e(S_1 + S_2 f_2 R_4 + S_3(f_3 R_4)^2 + S_4 R_4^3 + \ldots). \quad (7)$$

The parameterization given by equations (4), (5) or (7) can be written in matrix form $\boldsymbol{\mu} = \mathbf{S}\mathbf{m}$. Prediction is the forward calculation of $\boldsymbol{\mu}$ based upon knowledge of matrix $\mathbf{S}$ and the vector of mixture parameters $\mathbf{m}$. The model coefficients S_k can be obtained by fitting the polynomial of equation (2) to the cross-section tabulations. We have used the Lawrence Livermore National Laboratory (LLNL) (Cullen *et al.*, 1989; Boone & Chavez, 1996) and the National Institute of Standards (NIST) tabulations (Hubbell & Seltzer, 1995), with numerical results presented in the appendix of Midgley (2004). A complementary method uses μ measurements for different mixtures of known density and composition, to write linear simultaneous equations based upon equation (4). We use *SVDFIT.C* (Press *et al.*, 1992) to solve for the coefficients S_k. DEXA and MEXA use knowledge of $\mathbf{S}$ and measured $\boldsymbol{\mu}$ to estimate the material parameters N_e and R_4 by solving non-linear equations based upon equation (7). For this purpose we use an algorithm (Midgley, 2013) based upon the Levenberg–Marquardt method (Press *et al.*, 1992).

2.2. Calculation of the mass energy absorption coefficients for tissues

The compositional dependence of the energy absorption coefficient μ_{en} can also be described using a polynomial. DEXA delivers N_e and R_4 allowing μ_{en} to be calculated *via* equation (7). An estimate for the mass energy absorption coefficient is obtained by dividing by the mass density ρ related to N_e *via*

$$N_e = \rho\left(\frac{\overline{Z}}{\mathrm{MW}}\right), \quad (8)$$

where the ratio of average atomic number to molecular weight MW is 0.535 ± 0.025 mol g^{-1} for body tissues, and can be represented as a function of R_4:

$$\left(\frac{\overline{Z}}{A}\right) = (a_0 + a_1 R_4 + a_2/R_4 + a_3/R_4^2), \quad (9)$$

where $a_0 = 0.8029$, $a_1 = -0.01433$, $a_2 = -1.567$ and $a_3 = 3.645$ for body tissues. Thus the mass energy absorption coefficient is evaluated as
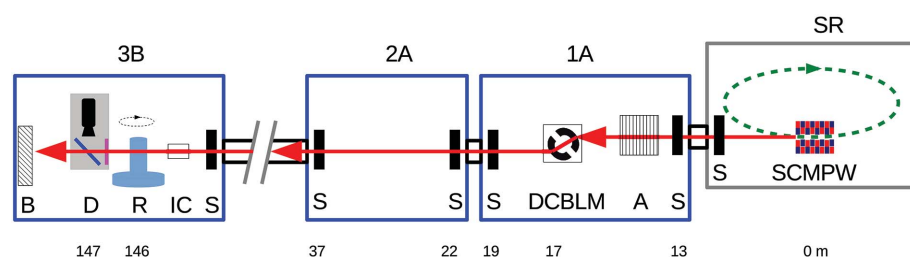
$$\left(\frac{\mu_{en}}{\rho}\right) = \left(S_{en1} + S_{en2} f_2 R_4 + S_{en3} f_3^2 R_4^2 + S_{en4} R_4^3 +\right)\left(\frac{Z}{A}\right). \quad (10)$$

2.3. IMBL instrumentation for mono-energetic CT

The Australian Synchrotron storage ring is operated at 3 GeV and utilizes top-up mode to compensate for the beam half-life (approximately 30 h) to maintain a current near 200 mA. The IMBL source is superconducting multipole wiggler radiation with a broad spectrum of energies extending beyond 100 keV and with a total radiative power of several tens of kW (Stevenson *et al.*, 2010, 2012).

The experimental configuration is illustrated in Fig. 1. The beam was filtered by the in-vacuum attenuators located in hutch 1A (thickness 5 mm graphite and 0.5–3.5 mm Al; oriented at 45° to give $\sqrt{2}$ longer path lengths), plus air and beryllium windows in hutches 2A and 3B. Beam energy selection used a dual-crystal bent Laue monochromator (DCBLM) where the mechanical bending serves to refocus the divergent beam. This configuration cannot maintain focus whilst one crystal is detuned, for example, to reject harmonic radiation. Beam energy is calculated *via* the Bragg equation, with the energy angle calibration being confirmed prior to the experiment by scanning across K-absorption edges in a series of metal attenuators (Zr to Sb). The available flux decreases at higher energies, and the useable energy range is approximately 20–80 keV. The beam is a broad fan that was collimated to a beam area of approximately 100 mm wide by 5 mm high. At the time of the experiment, a mechanical arm controlling bending of the second crystal had become detached, thereby compromising the ability to focus the beam.

The experiment was conducted in hutch 3B at 146 m from the source using the Ruby detection system (Hall *et al.*, 2013), which comprises a luminescent screen, optical coupling *via* mirror and lens (Nikon Micro-Nikkor 105 mm f2.8 macro) and a CMOS camera (PCO Edge, 2560×2160 pixels with native size 6.5 µm) that is located outside of the primary beam. We used the thickest available screen, a Gd_2O_2S:Tb phosphor taken from a mammography film cassette (Kodak Min-R), with screen coating weight 31.7 mg cm^{-2} or 43 µm thickness (Liaparinos *et al.*, 2006). The detector was operated at near-maximum pixel size of 45 µm and field of view 108 mm by 36 mm, and placed 100 cm behind the rotation stage, whereby the coarse

Figure 1
Schematic showing the IMBL configuration for CT, with distances from the source in metres. From right to left: the electron storage ring (SR) enclosure with superconducting multipole wiggler (SCMPW), shutters and/or slits (S), hutch 1A with beam attenuators (A) and double-crystal bent Laue monochromator (DCBLM), experimental hutch 2A and hutch 3B with ion chamber (IC), sample-rotation stage (R), Ruby detection system (D) and beam stop (B).

angular resolution minimizes the influence of refraction contrast (Midgley, 2007) in the raw CT projections.

Data acquisition used the Australian Synchrotron Experimental Physics and Industrial Control System (EPICS) to rotate the sample, control the frame grabber and camera *via* a plugin for *ImageJ*, and save data as 16 bit TIFF files. Data acquisition rates are 50 fps (20 ms frame^{-1}) for the camera, 35 fps (29 ms frame^{-1}) for the frame grabber and 3 fps (330 ms frame^{-1}) for EPICS. At the time of this experiment, frame averaging was not supported. Thus each frame was 330 ms involving 20 ms (6%) camera time, 29 ms (9%) data transfer and 270 ms (83%) of unused beam time. CT data acquisition used continuous rotation over 180° with the beam fully exposed for the duration.

The incident beam was monitored by an ADC IC-105 free air ionization chamber (Advanced Design Consulting USA Inc., Lansing NY) as described by Crosbie *et al.* (2013) with 60 mm path length, 11 mm electrode gap and approximately 150 mm width. In addition, a collimated silicon diode detector was monitoring scattered radiation arising from primary beam interactions with air in the experiment hutch.

2.4. Sample details

Two phantoms were assembled containing liquids of known density and composition. The phantoms comprised a polypropylene cylindrical container (internal diameter 62 mm, length 100 mm) with Perspex insert to support a hexagonal array of 19 polypropylene shell vials (outer diameter 8 mm, length 40 mm) containing aqueous ethanol and salt solutions. Sample details are listed in Table 1, with R_4 spanning that of tissues from fat to adult cortical bone.

The aqueous solutions of varying concentrations were prepared by mixing a known mass of solute and solvent, and measuring their density with a 10 ml laboratory pycnometer. Uncertainties for the hydration state of the solute can introduce systematic errors to estimates for concentration. These were reduced by consulting published tabulations of mass density against concentration (Nikolski, 1964; Perry & Green, 2007). The phantoms are water based with similar dimensions to the biological sample to ensure similar scattering properties. Their electron density and compositional parameters were calculated as follows. Weight fractions were converted to an approximate chemical formula cf(Z) with the contribution from the least abundant element rounded to unity. The molecular weight is

$$\text{MW}_{\text{mix}} = \sum_Z \text{cf}(Z)A(Z). \tag{11}$$

The atomic density of each element in units of mol cm^{-3} is

$$n_a(Z) = \frac{\rho}{\text{MW}_{\text{mix}}}\text{cf}(Z), \tag{12}$$

and the mixture parameters are calculated *via* equation (3).

An *ex vivo* biological specimen (Wistar rat) was also subject to CT for DEXA. The animal was bred according to local regulations and codes of practice governing biological research facilities. The carcass was retrieved from a batch of

Table 1
Details of the liquid samples showing solubility (g per 100 ml), an alphanumeric label, mass density ρ (g cm^{-3}), concentration (g per 100 ml), N_e (mol cm^{-3}) and R_4.

Solute	Solubility	Label	ρ	Conc.	N_e	R_4
Ethanol	Soluble	K4	0.782	100.18	0.441	6.36
		K3	0.880	63.14	0.494	6.79
		K2	0.917	47.17	0.513	6.96
Water		W	1.000	100.00	0.555	7.43
NaCl	35.9	A1	1.048	6.94	0.576	8.42
		A2	1.092	12.85	0.596	9.12
		A3	1.147	19.93	0.619	9.85
		A4	1.158	21.30	0.624	9.98
NaH$_2$PO$_4$	73.0	C1	1.098	12.91	0.602	8.05
		C2	1.185	23.16	0.643	8.49
		C3	1.222	27.24	0.660	8.66
		C4	1.273	32.59	0.684	8.87
MgCl$_2$	54.6	D1	1.031	4.00	0.569	8.13
		D2	1.082	9.95	0.593	9.01
		D3	1.109	12.98	0.605	9.40
		D4	1.123	14.53	0.612	9.59
MgSO$_4$	37.0	E1	1.053	5.33	0.581	7.79
		E2	1.123	11.78	0.616	8.19
		E3	1.168	15.72	0.638	8.42
		E4	1.204	18.75	0.656	8.59
KCl	34.2	F1	1.034	5.58	0.570	8.79
		F2	1.076	11.90	0.588	9.97
		F3	1.123	18.66	0.608	10.99
		F4	1.140	21.03	0.616	11.31
KH$_2$PO$_4$	22.6	G1	1.026	3.67	0.567	7.90
		G2	1.055	7.66	0.581	8.35
		G3	1.092	12.76	0.598	8.88
		G4	1.117	16.21	0.610	9.20
CaCl$_2$	74.5	H2	1.176	19.88	0.637	11.23
		H3	1.230	25.28	0.662	11.93
		H4	1.294	31.29	0.691	12.64
		H5	1.365	37.46	0.723	13.30

unallocated and thus surplus animals recently euthanized by submersion in carbon dioxide, sealed in a plastic zip-lock bag, placed in a cylindrical container, stored in a freezer held at 193 K, and returned after the experiment.

2.5. Experimental methods

The samples were placed on a Huber rotation stage. The *ex vivo* specimen was mounted in a PVC tube glued to a plastic board, which was joined with screws to the base plate of the rotation stage. During data acquisition, a liquid nitrogen filled dewar directed a stream of cold dry gas towards the body, thereby preventing the build-up of water ice and slowing the process of thawing to room temperature.

Prior to each CT scan, the presence of beam harmonics was investigated using the Ruby detector to measure transmission through a copper step wedge. This important quality control check investigates whether the exponential attenuation law holds for a range of sample thicknesses (Creagh & Hubbell, 1990). At energies below 35 keV, we identified harmonics that led to significant beam hardening with measured μ decreasing with thickness.

Projection data sets for CT were acquired for the phantoms and three regions of the frozen Wistar rat. Before and after each CT scan, series of dark-field images were acquired with the beamline shutters closed, followed by series of flat-field

images with the shutters opened and no sample in the beam. Data acquisition used a beam collimated to 74 mm by 2.4 mm and the camera operated to acquire just one frame per view, acquiring 1100 projections over 180°, in 360 s at two photon energies 35 and 60 keV.

2.6. Pre-processing corrections and CT reconstruction methods

The transmitted intensity signal recorded by the camera was subject to the following corrections: subtraction of the dark field, division by the flat field to remove spatial non-uniformities, and taking the logarithm to express the result as the ray-sum, representing the sum of μ and thickness t along the projection line through the sample. As the beam profile can change over time, flat-field images were collected before and after each CT scan, and their weighted average was used to estimate the flat field for each view.

Since the beam divergence across the detector was less than 0.1°, CT reconstruction utilized parallel-beam geometry filtered back projection (FBP) with the filtration step implemented as a real-space convolution. A variety of apodization functions (Ramachandran & Lakshminarayanan, 1971; Shepp & Logan, 1974; Webb, 1982, 1988) were available to attenuate the high-frequency noise that is otherwise amplified by the ramp filter during FBP. The back-projection step provided three interpolation options: nearest neighbour (NINT), linear (LINT) and spline (SPLINT) interpolation (Press *et al.*, 1992). In §3.4 we compare results for SPLINT against LINT. Pre-processing and CT reconstruction were coded using the C programming language. Quantitative analysis of quality control measurements with the camera and the CT results was conducted using *ImageJ* (Rasband, 1997; Schneider *et al.*, 2012).

3. Results

DEXA requires quality control measures to minimize the influence of systematic and random errors. To this end, we investigated the influence of harmonic radiation, and assessed camera performance and the temporal stability of the incident beam. We also estimated the radiation dose delivered during each CT scan. The present detection system requires data pre-processing to reduce noise. The model coefficients S_k in equations (2) to (7) are estimated from measurements of μ with the phantoms of known density and composition. DEXA accuracy was assessed using the same data set. In addition, the biological sample was subject to DEXA and the results used to predict μ and (μ_{en}/ρ) at other photon energies.

3.1. Estimation of harmonics content

Transmission measurements with the copper step wedge were expressed as ray-sums and fitted to a quadratic function with zero offset,

$$\begin{aligned} 35\,\text{keV} \quad & \mu t = 66.3t - 85.6t^2, \\ 60\,\text{keV} \quad & \mu t = 14.6t - 2.47t^2, \end{aligned} \tag{13}$$

where mono-energetic μ for copper (Hubbell & Seltzer, 1995) is 63.0 cm^{-1} (35 keV) and 14.2 cm^{-1} (60 keV). Figs. 2(a) and 2(b) show the difference between measured ray-sums and the linear term in this model representing the relative error in forming the ray-sums. The systematic error is larger for thicker and higher-Z materials.

The harmonic content was estimated as follows. We assumed a beam with the principal and third harmonic only, with relative intensities $I_0(E_0)$ and $I_0(3E_0)$. This model was fitted with NIST attenuation coefficients for copper against our ray-sum measurements. The results show that measured harmonic contamination relative to the principal is 1.0% at 35 keV and 1.5% at 60 keV. This information was used to calculate the relative error in estimating ray-sums (Midgley, 2006) for tissues as shown in Figs. 2(c) and 2(d).

3.2. Analysis of the camera dark signal and flat field

The camera dark signal was uniform and without structure, stable over time and independent of beam energy, with a mean pixel value of 100 and a noise-to-signal ratio (NSR) of 3.2%, evaluated as the ratio of standard deviation to mean.
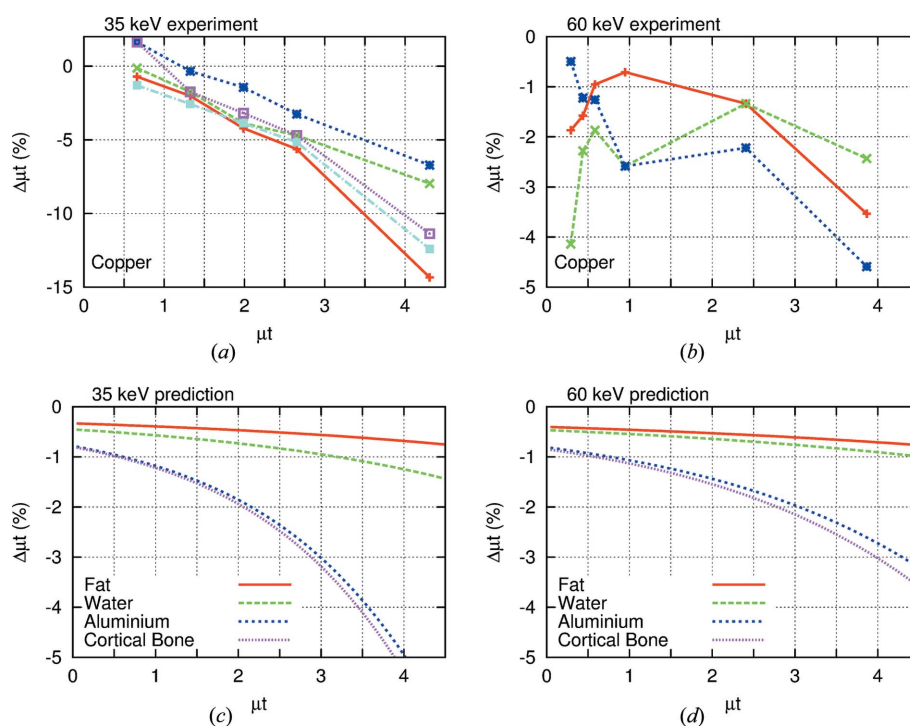
Figure 2
Difference between ray-sums for mono-energetic radiation and (a), (b) multiple measurements of ray-sums for copper, and (c), (d) predicted ray-sums for tissues.

Table 2
Fractional change (as %) between 30-frame average of flat-field images acquired before and after each CT scan.

E	Sample	Mean	Standard deviation
35 keV	L1a	0.6	0.3
	L2a	3.3	1.3
	Abdomen	6.9	2.2
	Pelvis	−2.3	0.6
60 keV	L1a	−2.1	2.5
	L2a	−1.9	2.4
	Abdomen	2.3	0.2
	Pelvis	−2.2	1.2

Table 3
Measured ionization current (I_{ic}), calculated air kerma rate using equation (14), ratio of air kerma to fluence *via* equation (1), ratio of mass energy absorption coefficients and estimate for the incident fluence rate [millions of photons (Mph) per unit area per unit time].

Parameter	Units	35 keV	60 keV
I_{ic}	(nA)	18.4	4.2
dK_{air}/dt	(mGy s^{-1})	42	9.7
K_{air}/φ_o	(μGy mm^2 Mph^{-1})	55	30
$(\mu_{en}/\rho)_{air}^{water}$	ratio	0.77	0.88
I_o	(Mph mm^{-2} s^{-1})	0.764	0.323

The incident beam was collimated to 1618×38 pixels (72.8 mm by 1.7 mm). Flat-field images did not contain bright or dark spots that can arise from diffraction by the beamline optics (Black & Long, 2004). The spatial profile across the flat field was brightest in the centre, falling by 10–30% at the edges, due to a mechanical fault that compromised the ability to focus the beam and the absence of a shading correction for the camera lens. For a region of interest (ROI) occupying the centre third of the flat field, the NSR was 7–12% at 35 keV and 4–8% at 60 keV.

The temporal stability of the flat field was quantified by subtracting images summed over 30 frames before and after each CT scan (6–10 min apart), and dividing by the mean. As the storage ring was operated in top-up mode, it was not necessary to apply a decay correction. Subtracted flat-field images did not contain structure, indicating good spatial stability over the duration of a CT scan. Results are summarized in Table 2, where the average difference ranges from 0.5% to a few percent. Noise in the projections propagates into the CT reconstruction and is considered in detail in §3.4.

3.3. Beam dosimetry

The ionization chamber measures the rate of charge production $I_{ic} = dQ/dt$ in the irradiated volume containing the mass of air m_{air}. Assuming that the corrections for electron energy loss and ion recombination are unity, the air kerma rate for the incident primary beam is estimated *via*

$$\frac{dK}{dt} = \frac{I_{ic}}{m_{air} w_{air}}, \tag{14}$$

where $w_{air} = 34$ eV is the mean ionization energy for air (Greening, 1981). We use equation (1) expressed as the ratio of air kerma to beam fluence (averaged over the total beam area) to convert the measured air kerma rate to an estimate for the beam fluence rate.

The irradiated volume has a length of 60 mm, and the camera images show that the width and depth are 1635×55 rectangular pixels of size 45 µm. It contains a mass of air of 1.28×10^{-5} kg based upon a dry air density of 1.205×10^{-6} kg cm^{-3} and assuming that the chamber correction factor for departures from standard temperature and pressure is unity. Table 3 summarizes the ion-chamber measurements and their conversion to beam fluence. The air

kerma per unit fluence was calculated for a mono-energetic beam *via* equation (1) using the mass attenuation coefficient for air from the NIST tabulation (Hubbell & Seltzer, 1995). The air kerma rate was estimated *via* equation (13) leading to an estimate for the incident fluence rate in SI units and expressed per pixel per frame (for 494 pixels per mm^2 and 0.33 s per frame).

Each CT scan acquired 1100 views in 6 min, delivering an air kerma at the sample of 15 Gy at 35 keV and 3.5 Gy at 60 keV. For a uniform cylindrical sample of diameter $2R$, the entrance skin air kerma (ESAK) is reduced due to sample rotation by a factor of $\exp(-2R\mu/\pi)$, which is approximately 0.5 for the samples considered in this study. The beam is a narrow fan, with a BSF $\simeq 1.10$ (Harrison, 1982), so the absorbed dose to the skin is approximately 7 Gy at 35 keV and 2 Gy at 60 keV.

3.4. CT noise-reduction strategies

The ratio of random errors for the ray-sum μt to those for the incident-beam fluence I_o is given by propagation of errors analysis (Rose & Shapiro, 1948; Nördfors, 1960; Midgley, 2006) leading to the expression

$$\frac{(\sigma_{\mu t}/\mu t)}{(\sigma_{I_o}/I_o)} = \frac{1}{\mu t} \frac{\sqrt{[1 + \exp(+\mu t)]}}{1 - B \exp(+\mu t)}, \tag{15}$$

where the detector records a background (or dark) signal $I_B = BI_o$. No background signal ($B = 0$) leads to a broad minimum, where the optimum thickness for CT is $0.5 \leq \mu t \leq 5.0$. Predicted results are shown in Fig. 3 with crosses denoting the average ray-sums for our samples. Our measurements were for radiologically thin samples, where the mean ray-sum $\overline{\mu t}$ is 0.6–1.3 and the error amplification factor is 1.8–3.6. The mean pixel value for the flat field is 28000 at 35 keV and 6400 at 60 keV, whilst the NSR (Table 4) for an average of 60 flat fields is approximately 10% at 35 keV and 5% at 60 keV. For FBP reconstruction with a top-hat apodization filter and LINT, the reconstructed NSR is 20–30%. The following pre-processing strategies were employed to improve the reconstructed image quality.
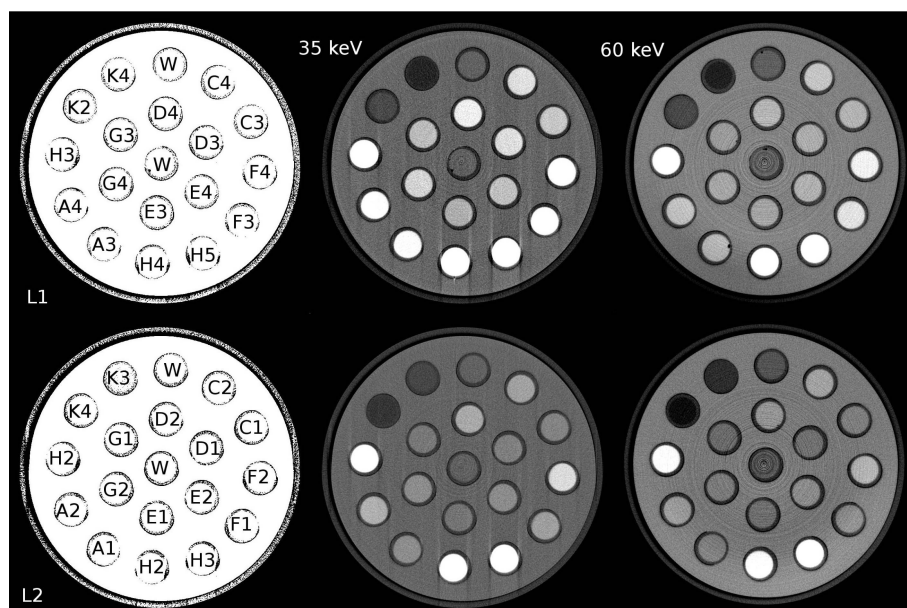
The FBP reconstruction replaced the top-hat apodization factor (Webb, 1988) with the Hamming window to suppress the influence of noise amplification by the ramp filter, improving the reconstructed NSR by a factor of 0.6. The interpolation process for back projection used SPLINT over
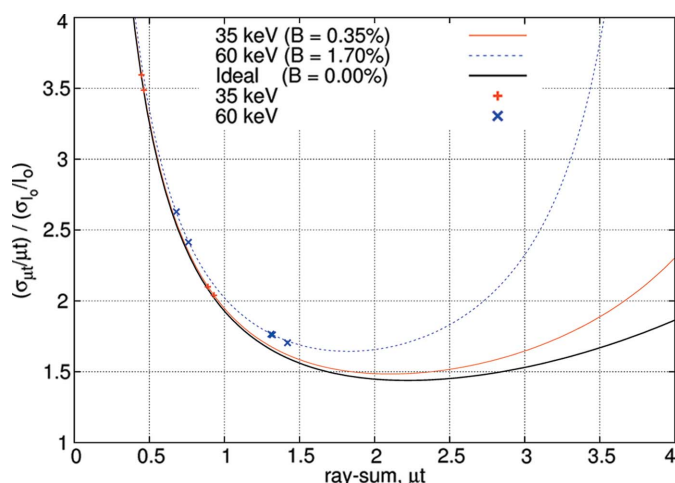
Figure 3
The ratio of errors for the ray-sum μt to that of the incident beam, evaluated *via* equation (15) and for the average ray-sums (points) considered in this study.

Noise was reduced by median filtering with mask size $(2M + 1)^2$.

Parameter	Mask size	35 keV		60 keV	
(*a*)					
Phantom		L1a	L1b	L1a	L1b
Flat field	Raw data	8.8	10	8.0	7.2
CT recon.	Raw data	16	12	6.5	5.6
Flat field	(5×5)	2.7	3.6	2.4	2.3
CT recon.	(5×5)	6.5	6.0	3.5	3.6
(*b*)					
Wistar rat		Abdomen	Pelvis	Abdomen	Pelvis
Flat field	Raw data	9.4	12	3.6	5.0
CT recon.	Raw data	33	35	18	19
CT recon.	(3×3)	11	12	7	7
CT recon.	(5×5)	6.1	6.3	3.5	3.7
CT recon.	(7×7)	4.1	4.2	2.6	2.5

Table 5
Model coefficients S_k [in units barn per electron$^{(k-1)}$] describing measured elemental cross sections *via* equation (2).

E (keV)	S_1	S_2	S_3	S_4
35	3.60×10^{-1}	-3.29×10^{-3}	-8.70×10^{-4}	6.53×10^{-4}
60	3.25×10^{-1}	5.33×10^{-3}	-8.86×10^{-4}	1.54×10^{-4}

LINT, further improving the reconstructed NSR by a factor of 0.8. We investigated two pre-processing strategies for filtering the raw data: pixel averaging by rebinning, and median filtering, with results presented in Table 4.

Rebinning to $(N \times N)$ pixels (results not shown) improves the NSR by $1/N$, but at the cost of reducing spatial resolution. The median filter was investigated using the algorithm *SELECT.C* of Press *et al.* (1992) with mask size $(2M + 1)^2$. Results presented in Table 4 show that the NSR is reduced (*i.e.* improved) as $1/M$. Mask sizes greater than $M = 2$ involve longer processing times with degraded spatial resolution. Therefore we used median filtering with $M = 2$ to pre-process all CT data sets, and improve the NSR by a factor of 0.5.
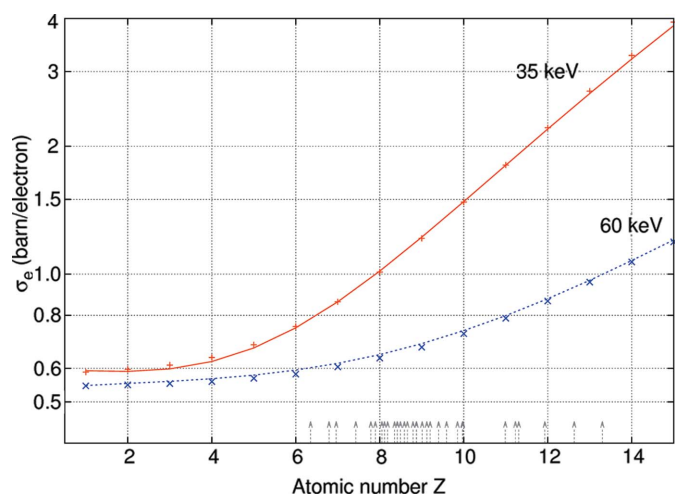
3.5. Beamline characterization for DEXA

Measured μ for materials in both phantoms illustrated in Fig. 4 were written as linear simultaneous equations according to equation (4) and solved for the model coefficients S_k using the methods outlined in §2.1. Predicted cross sections should increase with Z. This was not the case for $Z < 6$, which is outside of the sampled compositional range. Therefore the measured μ data were supplemented with NIST values for hydrogen and helium with mass density of unity. With this addition, the predicted cross sections were physically meaningful for the compositional range of interest hydrogen to calcium. Model coefficients S_k are presented in Table 5 and expressed in Fig. 5 as the atomic cross section per electron. Fig. 6 shows the differences between measurements and μ predicted by the model, where the full range is $\pm 2\%$ at 35 keV and $\pm 1.5\%$ at 60 keV.

3.6. DEXA results

Measurements for the liquid samples were subject to DEXA using equation (7) to write non-linear simultaneous equations that were solved for N_e and R_4 using the model coefficients S_k obtained in §3.5 and the methods

Figure 4
Central reconstructed slice for the phantoms L1 (upper row) and L2 (lower row) at 35 keV (centre) and 60 keV (right).
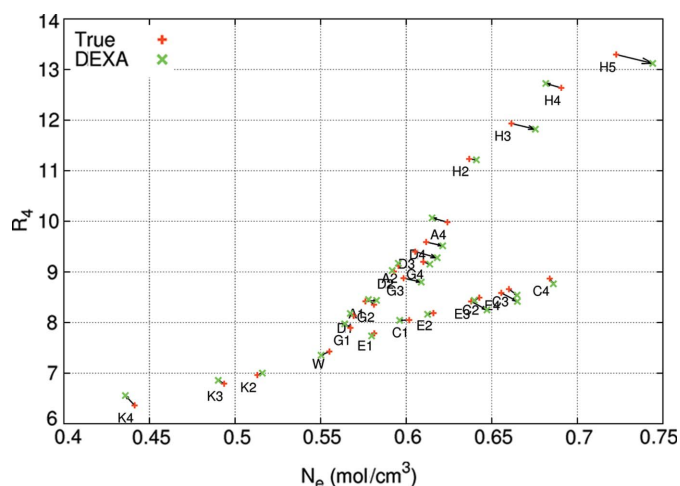
Figure 5
Elemental cross sections from the NIST tabulation (discrete points) and predictions (lines) using the model coefficients presented in Table 5. Arrows indicate values of R_4 for the salt solutions.
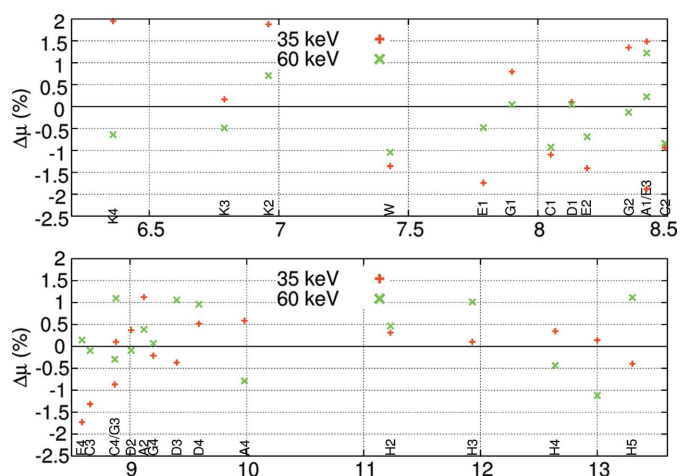
Figure 6
Differences between measured μ and values predicted by the model of equation (4) with $N = 4$ coefficients and using the cross sections shown in Fig. 5.

outlined in §2.1. The DEXA algorithm used an estimate for coefficients f_k based upon a parameterization of values for mixtures of lipid and water and for mixtures of water and compact bone (Midgley, 2013). Fig. 7 compares DEXA results for the phantoms against the known values for N_e and R_4.

The volumetric CT data sets for the biological sample were spatially co-registered using the *Advanced Normalization Tools* (ANTs) software package (Avantes *et al.*, 2011), and underwent the DEXA on a pixel-by-pixel basis. The scanned volume was too narrow in the axial direction to provide enough landmarks for full three-dimensional co-registration, so we used similar axial planes and a two-dimensional affine transformation. The DEXA results were rejected when outside the range $0.1 \leq N_e \leq 2.0$ and $5 \leq R_4 \leq 25$, by assigning the floating-point value 'not a number' (NAN). Results for the pelvis region are presented in Fig. 8.

Figure 7
DEXA results for the liquid samples compared against expectations based upon known density and composition, as summarized in Table 1.

3.7. Predicted interaction coefficients at other photon energies

In order to predict μ and (μ_{en}/ρ) for other beam energies, we used material parameters estimated *via* DEXA, the linear models of equations (4) and (10), and parameterization coefficients S_k obtained by fitting a polynomial to the tabulations (Midgley, 2004). The results for μ are presented in Fig. 9, and similar images are produced for (μ_{en}/ρ) with an example shown in Fig. 10(*c*). The images underwent quantitative analysis using circular ROI with diameters 2.5–8 mm. The DEXA results were expressed as the coordinates (N_e, R_4)
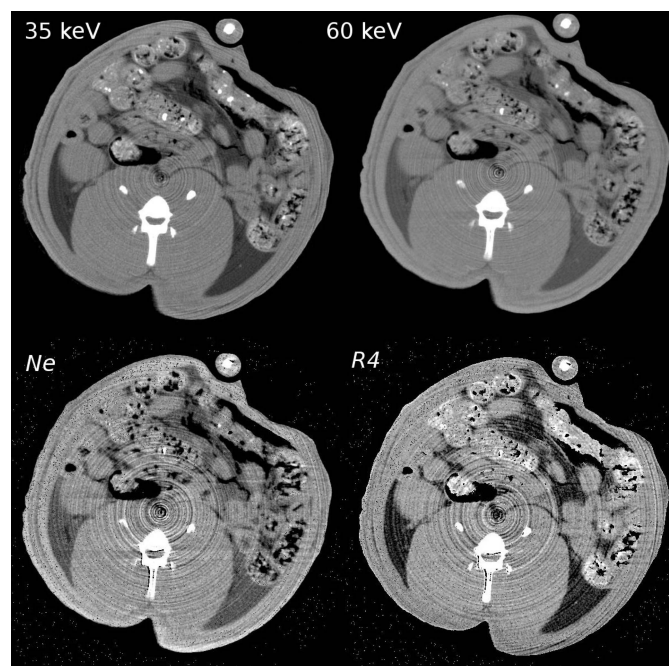
Figure 8
Co-registered slices for the Wistar rat pelvis (upper row) and DEXA results (lower row). The grey scales represent $\mu = 0$–1.6 cm^{-1} (35 keV), $\mu = 0$–0.6 cm^{-1} (60 keV), $N_e = 0.1$–1.0 mol cm^{-3} and $R_4 = 5.5$–13.5. The tail is folded along the abdomen and appears near 12 o'clock.
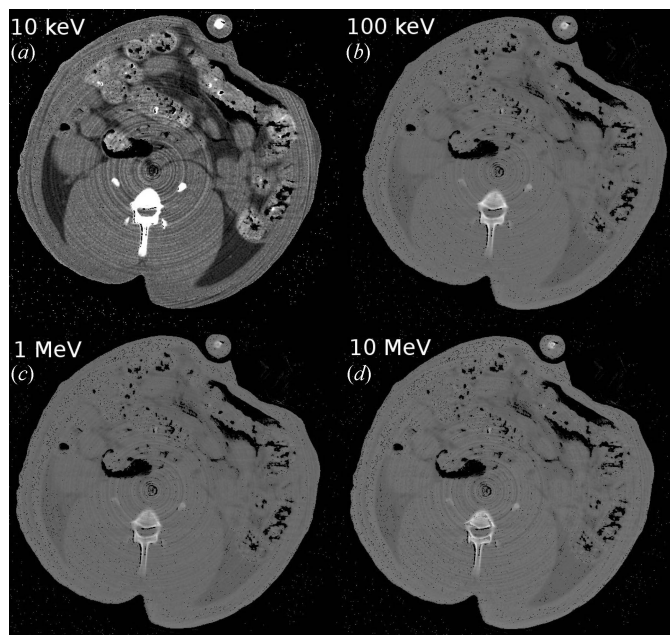
Figure 9
Maps of the predicted X-ray linear attenuation coefficients at (*a*) 10 keV (mean of all pixels excluding air is 3.1 cm^{-1}), (*b*) 100 keV (mean 0.79 cm^{-1}), (*c*) 1 MeV (mean 0.033 cm^{-1}) and (*d*) 10 MeV (mean 0.010 cm^{-1}).

as per Fig. 7 and are as follows: body of the spinal vertebrae (0.79 ± 0.06, 11.8 ± 0.5), muscle (0.57 ± 0.01, 7.5 ± 0.2) and peritoneal fat (0.51 ± 0.01, 6.6 ± 0.3). The measured tissue parameters are within the expected ranges for similar human tissues (for numerical values see the appendices of Midgley, 2011). Fig. 10 compares results for both μ and (μ_{en}/ρ) against values for similar human tissues evaluated using the mixture rule and NIST tabulation (Berger *et al.*, 1990).

4. Discussion

The raw projection data contained a significant amount of noise, some minor artefacts and systematic errors arising from harmonic radiation. The camera design emphasizes robustness and cost over detection efficiency, with the electronics protected from the onset of radiation damage by being located outside of the primary beam; this comes with the cost of weak optical coupling efficiency. The random error arising from noise in the detection system is 20–30% per frame, and propagates into the CT reconstruction. We suppressed this noise contribution by pre-processing with a median filter, using FBP reconstruction with a Hamming apodization window to attenuate high-frequency noise that would otherwise be amplified by the ramp filter, and by means of cubic spline interpolation during back projection. The NSR in each reconstructed slice (Table 4) is reduced from 10–30% to approximately 3–5%.

CT reconstructions for the phantom exhibited weak ring artefacts and linear streaks (see the reconstructions at 35 keV in Fig. 4). The rings arise from small changes in the beam profile that were not fully removed by the flat-field correction.

The causes were small temporal variations in the electron-beam current between top-up injections, and spatial variations arising from mechanical vibration of the monochromator. Differences between flat-field images acquired before and after each scan, listed in Table 2, indicate the magnitude of these influences is of the order of 1%. Data acquisition involves continuous sample rotation with asynchronous data transfer over a network, with a small and variable time lag before writing to disk. The lag only becomes apparent after many scans and for periods of increased network traffic, leading to the angular sampling range being marginally less than the required 180° (Webb, 1988), which produces linear streaks in the reconstructions.

Transmission measurements with the copper step wedge (Figs. 2*a* and 2*b*) identified 1.0% (35 keV) and 1.5% (60 keV) contribution from third-harmonic radiation. The camera detection efficiency falls at higher energies, reducing the influence of the third harmonic by 34% (105 keV/35 keV) and 9% (180 keV/60 keV), so the flux ratio for third harmonic to the fundamental wavelength is 5–10%. Figs. 2(*c*) and 2(*d*) quantify the systematic errors for tissues due to beam hardening by harmonic radiation. Propagation of errors analysis for random errors in ray-sum measurements is illustrated in Fig. 3 as the ratio of errors for the ray-sum to those for the incident beam. Both are small because our samples are radiographically thin with mean ray-sums of 0.7–1.4 at 35 keV and 0.5–0.9 at 60 keV. Third-harmonic radiation leads to measured ray-sums being underestimated, and for our samples the systematic errors are approximately −0.6% for soft tissues and −1.2% for bone-like materials.

CT measurements of the phantoms were used to obtain coefficients S_k describing the compositional dependence of atomic cross sections (Fig. 5), including some forward-scattered radiation as measured by the instrumentation. Synthetic data for hydrogen and helium with mass density of unity extend the compositional sampling below $R_4 = 6$ to avoid non-physical cross sections and thus ensure that the predicted values increase with Z. The goodness of fit is shown in Fig. 6, where the difference between measured and modelled μ is less than 1.2–2.4% with standard deviation 0.7–1.0%.

The same data was used to test the DEXA algorithm, with results presented in Fig. 7. Systematic and random errors in the μ measurements are shared amongst N_e and R_4 in the DEXA solution such that one is underestimated and the other overestimated. Propagation of errors analysis (Midgley, 2013) shows how these errors are shared in the DEXA solution. The error for R_4 is weighted by the fractional compositional cross-product (representing the relative contribution of all R_k coefficients to μ) which is a function of beam energy and composition. At 35–60 keV the fractional compositional cross-product is 0.20–0.05 for soft tissue and 0.7–0.4 for bone. In the present case the DEXA accuracy ($\Delta N_e/N_e$, $\Delta R_4/R_4$) spans the range (±1.4%, −1.9% to +3.2%) for soft tissues and (±2.3%, −1.9% to +0.9%) for bone-like materials. The absolute fractional differences for (N_e, R_4) have average values (0.8%, 1.0%) for soft tissue and (1.2%, 0.8%) for the bone-like materials.

Fig. 8 presents CT results for the pelvis CT scan of the *ex vivo* sample showing the lower intestine, fat, muscle, the spine, skin and the zip-lock bag. The intestines are filled with gas pockets and partially digested food, in particular Ridley AgriProducts mouse cubes, which consist of a mixture of grain, roughage and flakes of a mineral supplement containing 0.9% potassium and 1.2% calcium by weight. The DEXA maps for N_e and R_4 are similar due to the strong correlations between these quantities for biological tissues. This was exploited *via* the model parameters f_k, allowing the linear model of equation (5) with five or more material parameters to be rewritten as the non-linear model of equation (7), now a function of two variables. The DEXA results for N_e and R_4 span the expected range for each parameter. Regions of black denote NAN, which indicates that the DEXA algorithm has failed to deliver meaningful results for regions of gas (where μ is small), at boundaries (due to partial volume effects), and where the artefacts (*e.g.* ring artefacts) are strong. The failure at boundaries is accentuated by using two-dimensional spatial co-registration instead of full three-dimensional methods.

Calculations for μ and (μ_{en}/ρ) are presented in Fig. 9 and in Fig. 10 against predictions based upon the NIST and LLNL tabulations for similar human tissues. The results show reasonable agreement between predictions for rodent tissue and expectations for non-adult human tissues. The comparison supports the methodology outlined in this paper in using DEXA to characterize the electron density and composition for tissues, and to predict tissue interaction coefficients at arbitrary photon energies.

Dosimetry estimates (§3.2) are summarized in Table 3. For a typical CT scan with 6 min of CT data acquisition, the radiation absorbed dose delivered to the sample is substantial. Achieving lower-dose CT would involve reducing the photon flux (*e.g.* by lowering the wiggler magnetic field and/or operating the monochromators on the shoulder region of the rocking curve) and utilizing a detection system with thicker phosphor and more efficient optical coupling. In addition,
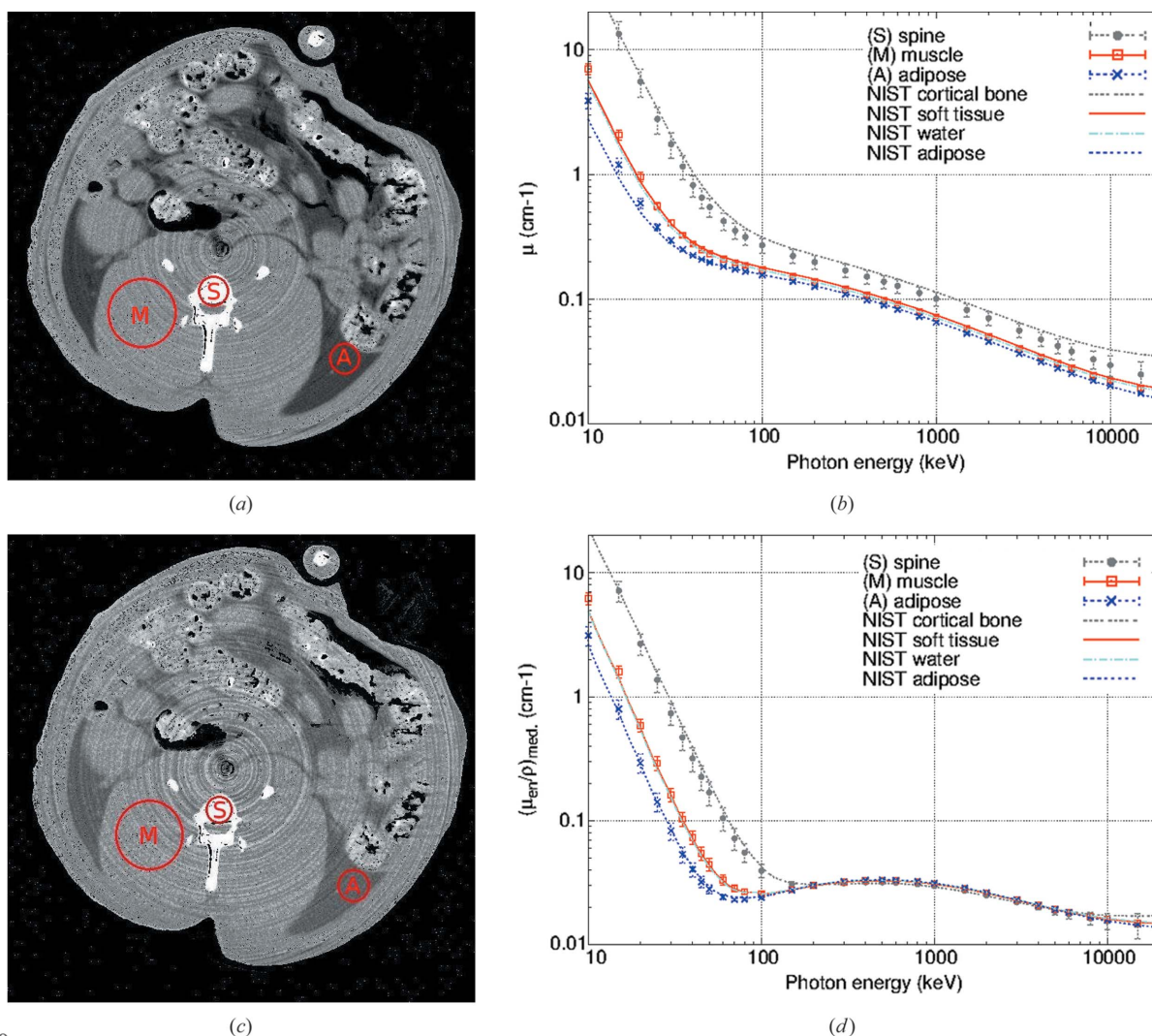
Figure 10
Images representing (*a*) linear attenuation and (*c*) mass energy absorption coefficients at 35 keV. Graphs compare model predictions (points) for regions of rodent (A) adipose, (M) muscle and (S) spine, against (lines) calculations using the mixture rule and tabulations (Cullen *et al.*, 1989; Hubbell & Seltzer, 1995; Boone & Chavez, 1996) for cortical bone (1 year-old child), soft tissue (ICRU 44 formulation), water and adipose (adult).

frame averaging may improve image quality, and the radiation dose might be further reduced by employing a fast shutter to block the beam while the system is busy with data transfer.

5. Conclusions

Necessary quality control steps for DEXA were outlined, and involve minimizing systematic and random errors in the raw data. It is important to test whether the exponential attenuation law holds (Creagh & Hubbell, 1990) by measuring transmission through a step wedge, whereby systematic errors become apparent when μ decreases with increasing attenuator thickness. Random errors arise from a variety of noise sources.

The IMBL with Ruby detection system was capable of CT at 20–80 keV with a near-parallel beam of size 110×2.4 mm. The experiment used 45 µm pixel size and acquired 1100 parallel projections over $180°$, which were reconstructed via FBP to 90 µm voxels. Systematic errors were identified in the projection data, which arose from the third-harmonic radiation with relative intensities of 5–10%. Their contribution was reduced to 1–1.5% of the recorded signal by the decrease in the detection efficiency at higher energies for the Gd_2O_2S phosphor. Our samples are radiographically thin with mean ray-sums of 0.5–1.5; thus the systematic errors in the measured ray-sums are low, from -0.6% for soft tissues to -1.2% for bone-like tissues. Weak optical coupling is a feature of the present detector design. As a consequence, noise in the flat-field images is approximately 10% at 35 keV and 5% at 60 keV, with temporal variations (Table 2) of a few per cent over the course of each CT scan. The radiation dose for each CT scan was estimated in §3.4 based upon air kerma rates measured by the in-beam ionization chamber. Strategies were suggested for reducing the beam intensity and dose rate for diagnostic imaging, and improving the detection system to capture more of the incident signal and to deliver better image quality.

Reconstruction by FBP to 90 µm voxels, using a top-hat apodization window (i.e. a pure ramp filter) with back projection based on linear interpolation delivered significant noise, approximately 30–20% at 35–60 keV. The situation was improved by pre-processing with a (5×5) median filter, replacing the top hat with a Hamming filter, and using spline interpolation. The respective noise improvements are $0.2 \times 0.6 \times 0.8 = 0.1$, reducing the reconstructed noise to 3–5%.

The system was characterized, using measurements with liquid samples of known density and composition to determine model parameters that describe the attenuation measured by the beamline. Here it is important to measure the mass density of each sample, and to choose compositions that fully span and evenly sample those of tissues characterized by $5.5 \le R_4 \le 13.3$. For the salt solutions, the amount of hydration water in the solute can be unknown, so we used tabulations of density and concentration to check our concentration estimates. A suitable algorithm was identified for solving the linear simultaneous equations based upon equation (4) and the results expressed as atomic cross sections at each beam energy. DEXA was tested against the same measurements, written as non-linear simultaneous equations based upon equation (7), which were solved using a modified Levenberg–Marquardt algorithm. Results were summarized as the difference from true values (ΔN_e, ΔR_4), approximately (0.8%, 1.0%) for soft-tissue-like samples and (1.2%, 0.8%) for bone-like samples. Torikoshi et al. (2003) conducted a similar synchrotron CT experiment with tissue substitute materials and liquids, to deliver N_e and R_4 within a few per cent of expected values. The important difference between these complementary approaches is the methods for obtaining the model coefficients: from the tabulations (Torikoshi et al., 2003; Midgley, 2004) versus via a 'calibration' experiment as used here.

The applications for DEXA are tissue characterization and the calculation of photon interaction coefficients at other beam energies. The latter were explored using CT scans at the same energies for a frozen biological sample and parameterization coefficients S_k obtained from published tabulations. Results were presented as volumetric maps representing N_e and R_4, and furthermore these results were successfully used to predict maps of μ and μ_{en} at energies from 10 keV to 20 MeV. This information is required for attenuation corrections, and is also used to calculate absorbed dose via equation (1) for diagnostic imaging across all modalities and for radiation therapy.

References

Avantes, B. B., Tustison, T. & Song, G. (2011). *Advanced normalisations tools (ANTS)*. Report. Penn Image Computing and Science Laboratory, University of Pennsylvania, PA, USA.

Berger, M. *et al.* (1990). NIST Report NBSIR 87–3597. National Institute of Standards and Technology, Bethesda, MD, USA.

Black, D. & Long, G. (2004). NIST Report SP 960–10. National Institute of Standards and Technology, Bethesda, MD, USA.

Boldeman, J. & Einfeld, D. (2004). *Nucl. Instrum. Methods Phys. Res. A*, **521**, 306–317.

Boone, J. & Chavez, A. (1996). *Med. Phys.* **23**, 1997–2005.

Creagh, D. C. & Hubbell, J. H. (1990). *Acta Cryst.* A**46**, 402–408.

Crosbie, J., Rogers, P. A. W., Stevenson, A. W., Hall, C. J., Lye, J. E., Nordström, T., Midgley, S. M. & Lewis, R. A. (2013). *Med. Phys.* **40**, 062103.

Cullen, D. *et al.* (1989). Report UCRL 50400. US Department of Commerce, Springfield, VA, USA.

Greening, J. (1981). *Fundamentals of Radiation Dosimetry*. Bristol: Hilger.

Hall, C. *et al.* (2013). *J. Instrum.* **8**, C06011.

Harrison, R. (1982). *Phys. Med. Biol.* **27**, 1465–1474.

Hubbell, J. *et al.* (1975). *J. Phys. Chem. Ref. Data*, **3**, 417–538.

Hubbell, J. & Överbö, I. (1979). *J. Phys. Chem. Ref. Data*, **8**, 69–105.

Hubbell, J. & Seltzer, S. (1995). Report NISTIR 5632. National Institute of Standards and Technology, Gaithersburg, MD, USA.

Jackson, D. & Hawkes, D. (1981). *Phys. Rep.* **70**, 169–233.

Liaparinos, P. F., Kandarakis, I. S., Cavouras, D. A., Delis, H. B. & Panayiotakis, G. S. (2006). *Med. Phys.* **33**, 4502–4514.

Midgley, S. (2004). *Phys. Med. Biol.* **49**, 307–325.

Midgley, S. (2005). *Phys. Med. Biol.* **50**, 4139–4157.

Midgley, S. (2006). *Radiat. Phys. Chem.* **75**, 936–944.

Midgley, S. (2007). *Phys. Med. Biol.* **52**, 5173–5186.

Midgley, S. (2011). *Phys. Med. Biol.* **56**, 2943–2962.

Midgley, S. (2013). *Phys. Med. Biol.* **58**, 1185–1205.

Nikolski, B. (1964). *Chemists' Reference Book*, Vol. III, 2nd ed. Moscow: Leningrad.

Nördfors, B. (1960). *Ark. Fys.* **18**, 37–47.

Perry, R. & Green, D. (2007). *Perry Chemical Engineers Handbook*, 8th ed. New York: McGraw Hill.

Press, W. S. A. T. *et al.* (1992). *Numerical Recipes in C. The Art of Scientific Computing.* 2nd ed. Cambridge University Press.

Ramachandran, G. & Lakshminarayanan, A. (1971). *Proc. Natl. Acad. Sci. USA*, **68**, 2236–2240.

Rasband, W. (1997). *ImageJ*. Report. US National Institute of Health, Bethesda, MD, USA.

Rose, R. & Shapiro, M. (1948). *Phys. Rev.* **74**, 1853–1864.

Schneider, C. A., Rasband, W. & Eliceiri, K. (2012). *Nat. Methods*, **9**, 671–675.

Seltzer, S. (1993). *Radiat. Res.* **136**, 147–170.

Shepp, L. & Logan, B. (1974). *IEEE Trans. Nucl. Sci.* **21**, 21–43.

Stevenson, A. W., Hall, C. J., Mayo, S. C., Häusermann, D., Maksimenko, A., Gureyev, T. E., Nesterets, Y. I., Wilkins, S. W. & Lewis, R. A. (2012). *J. Synchrotron Rad.* **19**, 728–750.

Stevenson, A. W., Mayo, S. C., Häusermann, D., Maksimenko, A., Garrett, R. F., Hall, C. J., Wilkins, S. W., Lewis, R. A. & Myers, D. E. (2010). *J. Synchrotron Rad.* **17**, 75–80.

Torikoshi, M., Tsunoo, T., Sasaki, M., Endo, M., Noda, Y., Ohno, Y., Kohno, T., Hyodo, K., Uesugi, K. & Yagi, N. (2003). *Phys. Med. Biol.* **48**, 673–685.

Webb, S. (1982). *Phys. Med. Biol.* **27**, 419–423.

Webb, S. (1988). *The Physics of Medical Imaging*. Bristol: Adam Hilger.

White, D. (1977). *Phys. Med. Biol.* **22**, 219–228.

Zhu, Y., Samadi, N., Martinson, M., Bassey, B., Wei, Z., Belev, G. & Chapman, D. (2014). *Phys. Med. Biol.* **59**, 2485–2503.